American Mineralogist, Volume 107, pages 31–42, 2022

Celleriite, $\square(Mn_2^{2+}Al)Al_6(Si_6O_{18})(BO_3)_3(OH)_3(OH)$, a new mineral species of the tourmaline supergroup

Ferdinando Bosi[1,*,‖], Federico Pezzotta[2], Alessandra Altieri[1], Giovanni B. Andreozzi[1], Paolo Ballirano[1,†], Gioacchino Tempesta[3], Jan Cempírek[4,*,‡], Radek Škoda[4], Jan Filip[5], Renata Čopjaková[4], Milan Novák[4], Anthony R. Kampf[6,§], Emily D. Scribner[7], Lee A. Groat[8], and R. James Evans[8]

[1]Department of Earth Sciences, Sapienza University of Rome, Piazzale Aldo Moro, 5, 00185 Rome, Italy
[2]Natural History Museum, Corso Venezia 55, 20121 Milan, Italy
[3]Department of Earth and Geoenvironmental Sciences, University of Bari "Aldo Moro", via Orabona 4, 70125 Bari, Italy
[4]Department of Geological Sciences, Faculty of Science, Masaryk University, 659 37 Brno, Czech Republic
[5]Regional Centre of Advanced Technologies and Materials, Czech Advanced Technology and Research Institute (CATRIN), Palacký University, Šlechtitelů 27, 783 71 Olomouc, Czech Republic
[6]Mineral Sciences Department, Natural History Museum of Los Angeles County, 900 Exposition Boulevard, Los Angeles, California 90007, U.S.A.
[7]Environmental Engineering and Earth Sciences, Clemson University, 445 Brackett Hall, 321 Calhoun Drive, Clemson, South Carolina 29634, U.S.A.
[8]Department of Earth, Ocean and Atmospheric Sciences, University of British Columbia, Vancouver, British Columbia V6T 1Z4, Canada

Abstract

Celleriite, $\square(Mn_2^{2+}Al)Al_6(Si_6O_{18})(BO_3)_3(OH)_3(OH)$, is a new mineral of the tourmaline supergroup. It was discovered in the Rosina pegmatite, San Piero in Campo, Elba Island, Italy (holotype specimen), and in the Pikárec pegmatite, western Moravia, Czech Republic (co-type specimen). Celleriite in hand specimen is violet to gray-blue (holotype) and dark brownish-green (co-type) with a vitreous luster, conchoidal fracture, and white streak. Celleriite has a Mohs hardness of ~7 and a calculated density of 3.13 and 3.14 g/cm^3 for holotype and its co-type, respectively. In plane-polarized light in thin section, celleriite is pleochroic (O = pale violet and E = light gray-blue in holotype; O = pale green and E = colorless in co-type) and uniaxial negative. Celleriite has trigonal symmetry: space group $R3m$, $Z = 3$, $a = 15.9518(4)$ and $15.9332(3)$ Å, $c = 7.1579(2)$ and $7.13086(15)$ Å, $V = 1577.38(9)$ and $1567.76(6)$ Å^3 for holotype and co-type, respectively (data from single-crystal X-ray diffraction). The crystal structure of the holotype specimen was refined to $R1 = 2.89\%$ using 1696 unique reflections collected with Mo$K\alpha$ X-ray intensity data. Structural, chemical, and spectroscopic analyses resulted in the formulas:

$^{X}(\square_{0.58}Na_{0.42})_{\Sigma 1.00}{}^{Y}(Mn^{2+}_{1.39}Fe^{2+}_{0.16}Mg_{0.01}Al_{1.14}Fe^{3+}_{0.01}Li_{0.28}Ti_{0.01})_{\Sigma 3.00}{}^{Z}Al_6[{}^{T}(Si_{5.99}Al_{0.01})_{\Sigma 6.00}O_{18}](BO_3)_3(OH)_3{}^{W}[(OH)_{0.65}F_{0.03}O_{0.32}]_{\Sigma 1.00}$ (for holotype)

and

$^{X}(\square_{0.51}Na_{0.49})_{\Sigma 1.00}{}^{Y}(Mn^{2+}_{0.90}Fe^{2+}_{0.50}Al_{1.36}Fe^{3+}_{004}Li_{0.17}Zn_{0.04})_{\Sigma 3.00}{}^{Z}Al_6[{}^{T}(Si_{5.75}B_{0.25})_{\Sigma 6.00}O_{18}](BO_3)_3(OH)_3{}^{W}[(OH)_{0.35}F_{0.17}O_{0.48}]_{\Sigma 1.00}$ (for co-type)

Celleriite is a hydroxy species belonging to the *X*-site vacant group of the tourmaline supergroup. The new mineral was approved by the Commission on New Minerals, Nomenclature and Classification of the International Mineralogical Association, proposal no. 2019-089.

In the Rosina pegmatite, celleriite formed an overgrowth at the analogous pole of elbaite–fluor-elbaite–rossmanite crystals during the latest stage of evolution of pegmatite cavities after an event of a pocket rupture. In the Pikárec pegmatite, celleriite occurs as an intermediate growth sector of elbaite, princivalleite, and fluor-elbaite.

Keywords: Celleriite, tourmaline, crystal-structure refinement, electron microprobe, Mössbauer spectroscopy, laser-induced breakdown spectroscopy, laser-ablation inductively coupled plasma mass-spectroscopy, Raman spectroscopy; Lithium, Beryllium, and Boron: Quintessentially Crustal

Introduction

Tourmaline minerals are reported to be the first boron minerals to have formed in Earth's crust and now are the most widespread of minerals for which boron is an essential constituent (Grew et al. 2016; Dutrow and Henry 2018). It is no surprise that this supergroup receives an ever-increasing interest from the geoscience community. Tourmaline minerals are complex borosilicates that have been extensively studied in terms of their crystal structure and crystal chemistry (e.g., Foit 1989; Grice and Ercit 1993; Ertl et al. 2002, 2018; Novák et al. 2004, 2011; Bosi and Lucchesi 2007; Bosi 2013, 2018; Henry and Dutrow 2011; Henry et al. 2011; Filip

* E-mail: ferdinando.bosi@uniroma1.it, jan.cempirek@gmail.com
† Orcid 0000-0001-9116-5393
‡ Orcid 0000-0003-3180-9534
§ Orcid 0000-0001-8084-2563
‖ Special collection papers can be found online at http://www.minsocam.org/MSA/AmMin/special-collections.html.

et al. 2012; Cempírek et al. 2013; Andreozzi et al. 2020).

A general chemical formula of tourmaline can be written as: $XY_3Z_6T_6O_{18}(BO_3)_3V_3W$, where X = Na, K, Ca, □ (=vacancy); Y = Al, Cr, V, Fe^{3+}, Mn^{3+}, Fe^{2+}, Mg, Mn^{2+}, Zn, Cu, Li, Ti; Z = Al, Cr, V, Fe^{3+}, Fe^{2+}, Mg; T = Si, Al, B^{3+}; B = B^{3+}; V = (OH), O; W = (OH), F, and O. Note that the non-italicized letters X, Y, Z, T, and B represent groups of cations hosted in the $^{[9]}X$, $^{[6]}Y$, $^{[6]}Z$, $^{[4]}T$, and $^{[3]}B$ crystallographic sites (letters italicized). The letters V and W represent groups of anions accommodated at the $^{[3]}$O(3) and $^{[3]}$O(1) crystallographic sites, respectively. The H atoms occupy the H(3) and H(1) sites, which are related to O(3) and O(1), respectively. According to the IMA-CNMNC guidelines (Bosi et al. 2019a, 2019b, and references therein): (1) the dominance of a chemical constituent (including vacancies and ion groups with the same valency state) of the dominant-valency state at a given structural site, and (2) the principle of valency-imposed double-site occupancy are the compositional criteria recommended to identify tourmalines (Henry et al. 2011). As a result, at least one structural site in a potential new tourmaline has to be dominated by a different chemical constituent from that present at the same site of an existing tourmaline.

Tourmaline-supergroup minerals are currently classified into three groups, *X*-site vacant, alkali, and calcic, based on the *X*-site occupancy (Henry et al. 2011). The *X*-site occupancy is usually related to both paragenesis and crystallization conditions of the rock in which tourmaline crystallized, and these relations may be used to reconstruct the host-rock thermal history (Henry and Dutrow 1996; van Hinsberg et al. 2011a, 2011b; Dutrow and Henry 2018; Bosi et al. 2018, 2019c; Ahmadi et al. 2019). A further level of classification into subgroups is based on charge arrangements at the *Y* and *Z* sites. Finally, in accord with the application of the dominant-valency rule, which in turn is followed by the application of the dominant-constituent rule (e.g., Bosi et al. 2019a), the dominant anion at the W position of the general formula allows distinguishing tourmalines into hydroxy-, fluor- and oxy-species (Henry et al. 2011).

A formal description of the new hydroxy-species celleriite is presented here. The mineral is named in honor of Luigi G. Celleri (1828–1900), from San Piero in Campo, Elba Island (Italy), for his contributions to the discovery of several new pegmatites during the second half of the 19th Century. He also gathered hundreds of magnificent specimens of tourmaline and associated minerals having scientific and collectible interest. Many of these specimens were part of the famous Raffaello Foresi and Giorgio Roster collections that today are part of the historic collections of the Mineralogy Museum of the University in Florence (Italy). Luigi G. Celleri also contributed by providing many of the pegmatitic minerals studied by Antonio D'Achiardi (1839–1902) of the University of Pisa (Italy). In 2012, the Mineralogical Museum of San Piero in Campo (Elba Island, Italy) was dedicated to Luigi G. Celleri. The new species and the new name have been approved by the Commission on New Minerals, Nomenclature and Classification (CNMNC) of the International Mineralogical Association (IMA), proposal no. 2019-089 (Bosi et al. 2020a).

Two specimens of celleriite were used to characterize the mineral: (1) the holotype specimen from the type locality Rosina pegmatite, San Piero in Campo, Elba Island (Italy), and (2) a co-type of celleriite from the Pikárec pegmatite, western Moravia (Czech Republic). The holotype was deposited in the collections of the Museo Universitario di Scienze della Terra (MUST), Sapienza University of Rome (Italy), catalog number 33287/403. Part of holotype specimen, used for measuring the refractive indices, was also deposited in the collections of the Natural History Museum of Milano (Italy), catalog number M38847. The co-type was deposited in the collection of the Moravian Museum, Brno (Czech Republic), catalog number A11375, and crystals used for measurement of optical properties are deposited in the collections of the Natural History Museum of Los Angeles County (U.S.A.), catalog number 75055.

Occurrence, appearance, physical and optical properties

The holotype specimen (San Piero in Campo, Elba Island, Italy) was discovered in the Rosina pegmatite and occurs as chemically homogeneous, millimeter to sub-millimeter zones within the analogous pole of a zoned tourmaline crystal (Fig. 1). Associated minerals are quartz, albite, K-feldspar, lepidolite, pollucite, petalite, tourmalines (elbaite, fluor-elbaite, and rossmanite), beryl, cassiterite, columbite-(Mn), "laumontite," "stilbite," and "heulandite." Its origin is related to miarolitic cavities occurring in the core zone of an asymmetrically zoned LCT-type pegmatite, which is hosted in monzogranite (Pezzotta 2000). San Piero in Campo is also the type locality of two other Mn-dominant tourmalines: tsilaisite and fluor-tsilaisite (Bosi et al. 2005, 2012, 2015). The holotype crystal occurs as a growth sector of violet (parallel to the **c**-axis) to gray-blue (perpendicular to the **c**-axis) color that is up to 3 mm in length. This sector

Figure 1. Dark celleriite overgrowth on the termination of an elbaitic crystal (1.7 cm tall) from the Rosina pegmatite (San Piero in Campo, Elba Island, Italy), with albite and quartz. One spessartine crystal is visible at the lower left of the specimen grown inside the quartz-albite aggregate. Photo by F. Picciani. (Color online.)

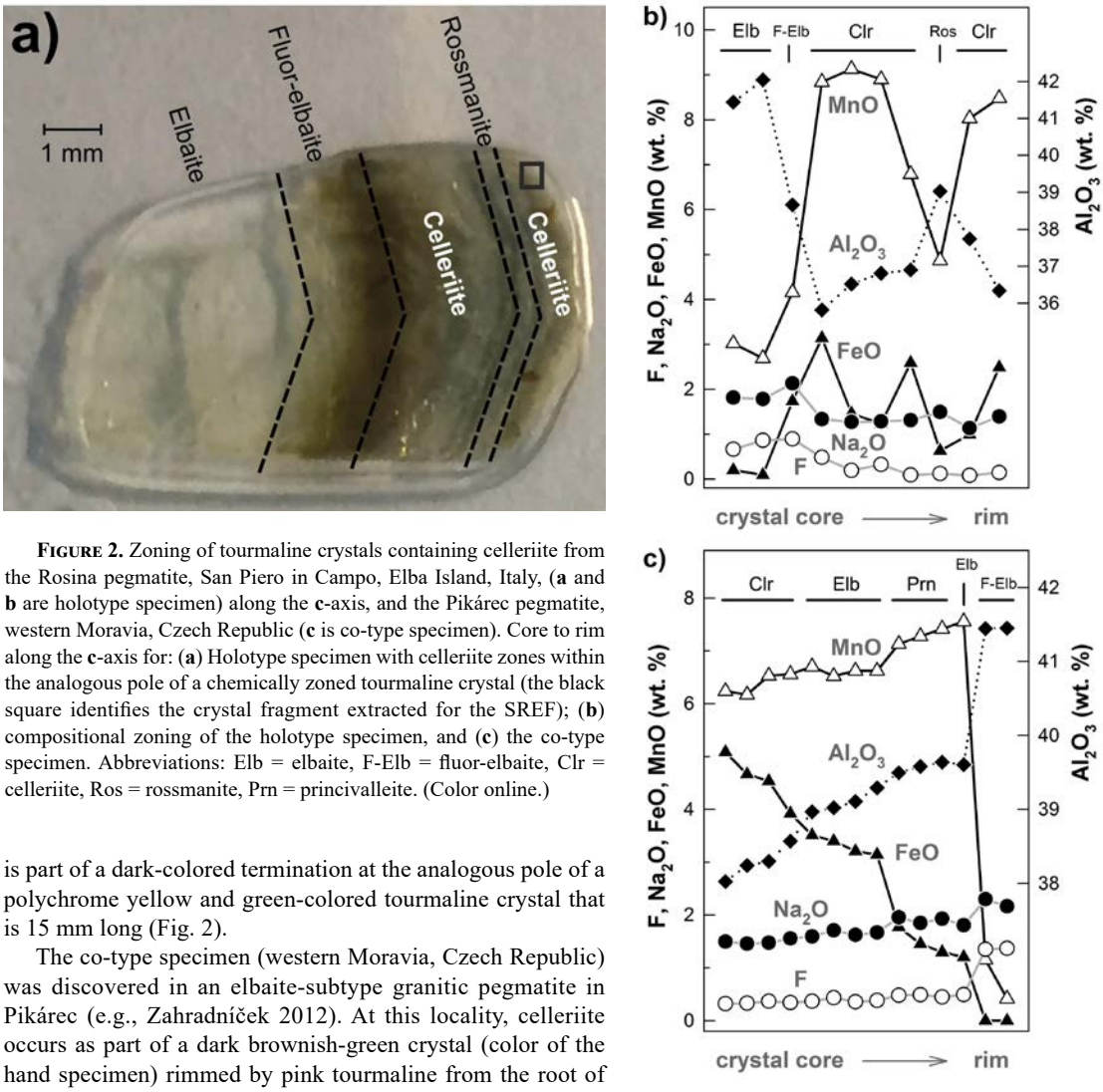

Figure 2. Zoning of tourmaline crystals containing celleriite from the Rosina pegmatite, San Piero in Campo, Elba Island, Italy, (**a** and **b** are holotype specimen) along the **c**-axis, and the Pikárec pegmatite, western Moravia, Czech Republic (**c** is co-type specimen). Core to rim along the **c**-axis for: (**a**) Holotype specimen with celleriite zones within the analogous pole of a chemically zoned tourmaline crystal (the black square identifies the crystal fragment extracted for the SREF); (**b**) compositional zoning of the holotype specimen, and (**c**) the co-type specimen. Abbreviations: Elb = elbaite, F-Elb = fluor-elbaite, Clr = celleriite, Ros = rossmanite, Prn = princivalleite. (Color online.)

is part of a dark-colored termination at the analogous pole of a polychrome yellow and green-colored tourmaline crystal that is 15 mm long (Fig. 2).

The co-type specimen (western Moravia, Czech Republic) was discovered in an elbaite-subtype granitic pegmatite in Pikárec (e.g., Zahradníček 2012). At this locality, celleriite occurs as part of a dark brownish-green crystal (color of the hand specimen) rimmed by pink tourmaline from the root of a pegmatite pocket; the crystal is ca. 3 cm long and 1.5 cm wide. Celleriite is associated with albite (variety cleavelandite), quartz, K-feldspar and other tourmaline-supergroup minerals: elbaite, fluor-elbaite and princivalleite $[Na(Mn_2^{2+}Al)Al_6(Si_6O_{18})(BO_3)_3(OH)_3O$; Bosi et al. 2020b]. It formed by fractional crystallization from B-rich residual albitic liquid in the final stage of the pegmatite magmatic crystallization. The pegmatite is a member of the Strážek pegmatite field (Novák and Cempírek 2010) in the central part of the Strážek Moldanubicum in the Moldanubian Zone of the Bohemian Massif. The pegmatite is associated with numerous other barren pocket pegmatites with smoky quartz and black tourmaline (Gadas et al. 2012), and several fractionated pegmatites that belong to the elbaite or lepidolite subtypes of the complex-type, rare-element class of granitic pegmatites (after Černý et al. 2012). The co-type crystal occurs as zones that are 2–5 mm wide and brownish-green to green in color, in a Mn-rich elbaite and princivalleite crystal, which can be distinguished only by chemical analysis. Celleriite is visually indistinguishable from the zones of tourmaline with the other composition. Other parts of the same crystal (termination and crystal core) are blue or violet, and their composition is oxy-schorl to foitite. Fluor-elbaite that rims the darker core is pale pink in thin section.

Celleriite has a vitreous luster, white streak, and no fluorescence. Its Mohs hardness is approximately 7. It is brittle with a conchoidal fracture, as inferred from the holotype crystal. Its calculated density, on the basis of the empirical formula and unit-cell volume refined from single-crystal X-ray diffraction data, is 3.13 g/cm^3 (holotype) and 3.14 g/cm^3 (co-type). Celleriite is transparent in thin section and pleochroic with O = pale violet and E = pale gray-blue (holotype) and O = pale green and E = colorless (co-type) in transmitted light. Celleriite is uniaxial negative with refractive indices as follows: for the holotype, ω = 1.643(1) and ε = 1.628(1) measured with a refractometer, and for the co-type, ω = 1.656(2) and ε = 1.627(2) measured with a spindle stage; white LED light (~5.500 K) was used for optical determinations in both cases. The mean index of refraction, density and chemical composition lead to excellent compatibility indexes (Mandarino 1981) for the holotype ($1 - Kp/Kc = 0.038$) and its co-type ($1 - Kp/Kc = 0.036$).

Experimental methods and results

General comment

For the Italian celleriite holotype specimen, crystal Structure REFinement (SREF), electron microprobe (EMP), and μ-laser-induced breakdown spectroscopy (μ-LIBS) data were all obtained from the same crystal fragment (black square in Fig. 2a). Complementary Mössbauer spectroscopy data (MS), refractive indices, and powder X-ray diffraction (XRD) data were acquired from a larger portion of the chemically zoned tourmaline crystal.

For the Czech co-type of celleriite, the crystal used for the SREF was extracted, using a microdrill-equipped microscope, from a domain previously examined using EMP and Raman spectroscopy, and just next to a laser ablation-inductively coupled plasma-mass spectroscopy (LA-ICP-MS) analytical spot. The Mössbauer spectrum and powder XRD pattern were obtained from a larger domain from the same compositional zone.

Single-crystal structure refinement

Holotype. A representative fragment crystal of celleriite from the Rosina pegmatite (San Piero in Campo, Elba Island, Italy) was selected for XRD measurements on a Bruker KAPPA APEX-II single-crystal diffractometer (Sapienza University of Rome, Earth Sciences Department), equipped with a charge-coupled device (CCD) area detector (6.2 × 6.2 cm active detection area, 512 × 512 pixels) and a graphite-crystal monochromator using Mo*K*α radiation from a fine-focus sealed X-ray tube. The sample-to-detector distance was 4 cm. A total of 2453 exposures (step = 0.2°, time/step = 20 s) covering a full reciprocal sphere with a redundancy of ~13 was collected. The intensity data were processed and corrected for Lorentz, polarization, and background effects using the APEX2 software program of Bruker AXS. The data were corrected for absorption using a multi-scan method (SADABS). No violation of *R*3*m* symmetry was detected.

Structure refinement was done using the SHELXL-2013 program (Sheldrick 2015). Starting coordinates were taken from Bosi et al. (2015). Variable parameters were scale factor, extinction coefficient, atom coordinates, site-scattering values (for *X*, *Y*, and *Z* sites), and atomic-displacement factors. Attempts to refine the extinction coefficient yielded values within its standard uncertainty; thus it was not refined. Neutral scattering factors were used for the cations and oxygen atoms. As for the atomic model refinement, the *X* site was modeled using the Na scattering factor. The *Y* site was refined by setting the Li occupancy to 0.28 atoms per formula unit (apfu) and allowing the remainder of the site to refine as Mn = (2.72 – Al) apfu. The *Z* site was modeled by Al vs. Mn. The *T*, *B*, and anion sites were modeled with Si, B, and O scattering factors, respectively, and with a fixed occupancy of 1 since refinement with unconstrained occupancies showed no significant deviations from this value. There were no correlations >0.7 between the parameters at the end of the refinement.

Co-type. A selected single-crystal of celleriite from Pikárec pegmatite (Moravia, Czech Republic) was studied using a Rigaku HighFlux HomeLab diffractometer (Masaryk University in Brno, CEITEC X-ray Diffraction and Bio-SAXS Core Facility) equipped with rotating anode X-ray source (multilayered optics, Mo*K*α radiation), partial χ axis goniometer and CCD detector (Saturn 724+ HG). The sample-to-detector distance was 3 cm. A total of 2048 exposures (step = 0.25°, time/step = 4 or 8 s) was collected with CrystalClear software and processed with CrysAlisPro. The structures were solved and refined using SHELX-2013 software package (Sheldrick 2015). Starting coordinates were taken from Cempírek et al. (2013). Variable parameters were scale factor, atom coordinates, site-scattering values (for *X*, *Y*, *Z*, and *T* sites) and atomic-displacement factors. The *X* site was modeled using the Na scattering factor. The *Y* site was refined by setting the Li occupancy to 0.17 apfu and allowing the remainder of the site to refine as Mn = (2.83 – Al) apfu. The *Z* and *T* sites were modeled by Al vs. Mn and Si vs. B, respectively. The *B* and anion sites were modeled with B and O scattering factors, respectively, and with a fixed occupancy of 1. The O(1) site was modeled with occupancy of O and F fixed to the value of the structural formula (see below). There were no correlations >0.72 between the parameters at the end of the refinement.

For the holotype specimen and its co-type, Table 1 shows selected bond lengths and a CIF[1] shows all structural data.

X-ray powder diffraction

Holotype. X-ray powder diffraction data were collected with a focusing-beam (Göbel mirror) Bruker AXS D8 Advance operating in transmission in θ-θ geometry. The instrument was fitted with a PSD VÅntec-1 with the acceptance angle set to 6° 2θ. The goniometer had a 250 mm radius. Data were measured using Cu*K*α radiation from a fine-focus sealed X-ray tube (Table 2). Unit-cell parameters refined using the Rietveld method from the powder data are as follows: a = 15.9330(2) Å, c = 7.13593(9) Å, and V = 1568.82(4) Å^3.

Co-type. The phase composition and structural data of pulverized tourmaline were determined by powder XRD with an X'Pert PRO diffractometer (Malvern Panalytical, Ltd) operating in Bragg-Brentano geometry with goniometer radius 240 mm. The diffractometer was equipped with an iron-filtered Co*K*α radiation source, programmable divergence and diffracted beam anti-scatter slits, and a fast PIXcel detector. The XRD pattern was measured in the 2θ range from 5 to 105° and the data were processed using HighScore Plus software in conjunction with PDF-4+ and ICSD databases (Table 3). Unit-cell parameters refined using the Rietveld method from the powder data are as follows: a = 15.9344(3) Å, c = 7.1313(2) Å, and V = 1568.08(6) Å^3.

Table 1. Selected bond lengths (Å) for celleriite from the Rosina Pegmatite, San Piero in Campo, Elba Island, Italy (holotype) and the Pikárec Pegmatite, Western Moravia, Czech Republic (co-type)

Sample	Holotype	Co-type
X-O(2) ×3	2.519(7)	2.534(3)
X-O(5) ×3	2.773(4)	2.7576(18)
X-O(4) ×3	2.837(5)	2.8151(19)
<*X*-O>	2.710	2.702
Y-O(2) ×2	1.971(2)	1.9714(9)
Y-O(1)	2.023(3)	2.0114(16)
Y-O(6) ×2	2.041(2)	2.0311(9)
Y-O(3)	2.134(3)	2.1390(16)
<*Y*-O>	2.030	2.026
Z-O(6)	1.874(2)	1.8648(9)
Z-O(8)	1.8857(19)	1.8823(9)
Z-O(7)	1.8866(19)	1.8771(8)
Z-O(8)′	1.924(2)	1.9171(9)
Z-O(7)′	1.9641(19)	1.9530(8)
Z-O(3)	1.9774(15)	1.9767(7)
<*Z*-O>	1.919	1.912
B-O(2)	1.360(5)	1.355(2)
B-O(8) ×2	1.380(3)	1.3823(12)
<*B*-O>	1.373	1.373
T-O(6)	1.607(2)	1.6097(9)
T-O(7)	1.6097(17)	1.6143(8)
T-O(4)	1.6209(10)	1.6217(5)
T-O(5)	1.6356(12)	1.6342(6)
<*T*-O>	1.618	1.620

Table 2. X-ray powder diffraction data (*d* in angstroms) for celleriite from the Rosina Pegmatite, San Piero in Campo, Elba Island, Italy (holotype)

I_{meas}	d_{meas}	d_{calc}	*hkl*	I_{meas}	d_{meas}	d_{calc}	*hkl*
5	7.9771	7.9665	110	38	2.0356	2.0422	223
45	6.3449	6.3385	101	38*		2.0354	152
20	4.9462	4.9600	021	8	2.0203	2.0183	161
13	4.6013	4.5995	030	3	1.9913	1.9916	440
60	4.2104	4.2106	211	26	1.9130	1.9143	342
88	3.9826	3.9832	220	5	1.9013	1.9000	701
55	3.4532	3.4544	012	5*		1.9000	351
10	3.3705	3.3726	131	6	1.8663	1.8665	413
4	3.1047	3.1057	401	7	1.8481	1.8482	621
10	3.0114	3.0111	410	2	1.8281	1.8276	710
55	2.9425	2.9448	122	1	1.8122	1.8125	612
5	2.8940	2.8936	321	5*	1.7696	1.7718	333
5	2.6088	2.6097	312	5		1.7693	104
100	2.5733	2.5739	051	3*	1.7258	1.7272	024
2	2.4801	2.4800	042	3		1.7254	072
2	2.4496	2.4492	241	3*		1.7254	532
16	2.3694	2.3786	003	3	1.6873	1.6863	262
16*		2.3679	232	17	1.6530	1.6534	603
17	2.3404	2.3411	511	17*		1.6534	063
2	2.2995	2.2997	060	11	1.6404	1.6406	271
2	2.2095	2.2095	520	13	1.5919	1.5933	550
11	2.1822	2.1829	502	6	1.5841	1.5846	404
10	2.1611	2.1618	431	6		1.5832	452
10	2.1088	2.1128	303				
10		2.1128	033				
10		2.1053	422				

Note: Whenever a single box is reported for the I/I_0 of a group of nearby reflections, the asterisk (*), if present, indicates the most intense one(s).

Table 3. X-ray powder diffraction data (*d* in anstroms) for celleriite from the Pikárec Pegmatite, Western Moravia, Czech Republic (co-type)

I_{meas}	d_{meas}	d_{calc}	*hkl*	I_{meas}	d_{meas}	d_{calc}	*hkl*
53	6.3264	6.3353	101	18	1.6524	1.6529	063
20	4.9533	4.9587	021	3	1.6524	1.6529	603
6	4.5952	4.5999	030	12	1.6402	1.6407	271
6	4.5952	4.5999	300	14	1.5930	1.5934	550
54	4.2060	4.2099	211	3	1.5834	1.5838	404
75	3.9801	3.9836	220	2	1.5827	1.5831	452
57	3.4497	3.4523	012	4	1.5449	1.5453	461
7	3.3699	3.3723	131	4	1.5237	1.5241	722
3	3.1035	3.1056	401	12	1.4972	1.4975	054
4	3.0094	3.0113	140	2	1.4714	1.4718	244
4	3.0094	3.0113	410	3	1.4487	1.4490	173
53	2.9417	2.9435	123	14	1.4470	1.4473	514
6	2.8918	2.8935	321	5	1.4464	1.4468	642
4	2.6075	2.6089	312	3	1.4184	1.4187	015
100	2.5725	2.5739	051	6	1.4174	1.4177	651
2	2.4480	2.4492	241	3	1.4030	1.4033	633
7	2.3760	2.3771	003	10	1.4015	1.4018	434
14	2.3663	2.3674	232	9	1.3546	1.3548	10.01
15	2.3400	2.3411	511	4	1.3402	1.3405	562
14	2.1816	2.1825	502	3	1.3276	1.3279	660
9	2.1610	2.1619	431	5	1.3233	1.3236	553
5	2.1109	2.1118	033	3	1.3220	1.3223	354
5	2.1109	2.1118	303	2	1.3178	1.3181	045
4	2.1041	2.1050	422	4	1.3096	1.3098	1.10.0
9	2.0405	2.0413	223	4	1.3096	1.3098	10.10
33	2.0343	2.0351	152	2	1.3038	1.3041	832
7	2.0176	2.0184	161	2	1.3002	1.3004	235
2	1.9910	1.9918	440	2	1.2756	1.2758	390
25	1.9134	1.9141	342	2	1.2756	1.2758	930
3	1.8994	1.9001	351	9	1.2669	1.2671	505
7	1.8652	1.8658	143	3	1.2548	1.2550	544
7	1.8476	1.8483	621	4	1.2353	1.2355	0.11.1
4	1.7706	1.7712	333	2	1.2073	1.2075	345
2	1.6857	1.6862	262	3	1.1799	1.1801	11.11
				6	1.1470	1.1472	10.13

Note: Only reflections with $I_{meas} \geq 2$ are reported.

Electron microprobe analysis

Holotype. The crystal used for the SREF was analyzed with a Cameca SX50 electron microprobe with wavelength-dispersive spectrometers (WDS mode) at the Istituto di Geologia Ambientale e Geoingegneria (Rome, Italy), CNR. The analytical conditions were: accelerating voltage 15 kV, beam current 15 nA, spot diameter 10 μm. Minerals and synthetic compounds were used as standards: wollastonite (Si, Ca), magnetite (Fe), rutile (Ti), corundum (Al), vanadinite (V), fluorphlogopite (F), periclase (Mg), jadeite (Na), orthoclase (K), sphalerite (Zn), rhodonite (Mn), metallic Cr, and Cu. The PAP routine was applied (Pouchou and Pichoir 1991). The results (Table 4) represent mean values of 10 spot analyses. V, Cr, Cu, Zn, Ca, and K were below detection limits (<0.03 wt%).

Co-type. The crystal used for the SREF was analyzed with a Cameca SX-100 electron microprobe (WDS mode) at Masaryk University in Brno, Czech Republic. The analytical conditions were: accelerating voltage 15 kV, beam current 10 nA, spot diameter 5 μm. Minerals and synthetic compounds were used as standards: sanidine (Si, Al), titanite (Ti), almandine (Fe), spessartine (Mn), gahnite (Zn), albite (Na), and topaz (F). The X-Phi matrix correction was applied (Merlet 1994). Chemical analysis is shown in the Table 4; no other elements heavier than F were detected.

Mössbauer spectroscopy

Holotype. Crystal fragments extracted from the Italian celleriite-rich portion of the zoned tourmaline were powdered to prepare a Mössbauer absorber containing 20 mg of tourmaline, which was loaded in an acrylic sample holder with diameter of 2 mm. Measurements were performed using a spectrometer with a ^{57}Co point source of 0.37 GBq (10 mCi) embedded in a Rh matrix. The spectrum was collected within 8 days in transmission mode at room temperature and at velocity between –4 to +4 mm/s, and was recorded in a multichannel analyzer with 512 channels. The velocity was calibrated with a 25 μm thick α-Fe foil. The obtained spectrum was fitted to Lorentzian line-shapes using the RECOIL 1.04 fitting program. The final fitting model consisted of four absorption doublets, three for $^{[6]}Fe^{2+}$ and one for $^{[6]}Fe^{3+}$, with hyperfine parameters (Table 5) consistent with those optimized by Andreozzi et al. (2008). The Fe^{2+}/Fe_{Tot} and Fe^{3+}/Fe_{Tot} ratios are quantified at 0.96(3) and 0.04(3), respectively (Fig. 3a).

Table 4. Chemical composition for celleriite from the Rosina Pegmatite, San Piero in Campo, Elba Island, Italy (holotype) and the Pikárec Pegmatite, Western Moravia, Czech Republic (co-type)

Sample	Holotype (10 spots)		Co-type
	Average	Range	(Single spot)
SiO_2 wt%	36.62(23)	36.19–36.96	35.51
TiO_2	0.09(2)	0.06–0.14	–
B_2O_3	10.62[a]	–	11.61[c]
Al_2O_3	37.08(43)	36.24–37.64	38.57
FeO_{tot}	1.19(25)	0.81–1.60	3.92
MnO	10.01(64)	8.80–11.15	6.56
ZnO	–		0.30
MgO	0.06(5)	0.01–0.09	–
Na_2O	1.34(16)	1.04–1.51	1.56
Li_2O	0.42[b]	–	0.26[c]
F	0.05(4)	0.00–0.13	0.34
H_2O	3.34[a]	–	3.10[a]
–O=F	–0.02		–0.14
FeO	1.14[d]		3.66[d]
Fe_2O_3	0.05[d]		0.29[d]
Total	100.79		101.62
Atomic fractions normalized to 31 anions			
Si (apfu)	5.994		5.754
Ti^{4+}	0.012		–
B	3.000		3.246
Al	7.154		7.365
Fe^{3+}	0.007		0.035
Fe^{2+}	0.156		0.496
Mn^{2+}	1.388		0.900
Zn	–		0.036
Mg	0.013		–
Na	0.424		0.489
Li	0.277		0.167
F	0.028		0.174
OH	3.651		3.350

Notes: Errors for oxides and fluorine are standard deviations (in parentheses); apfu = atoms per formula unit.
[a] Calculated by stoichiometry.
[b] Determined by μ-LIBS.
[c] Determined by LA-ICP-MS.
[d] Determined by Mössbauer spectroscopy.

Co-type. Tourmaline fragments extracted from the cut sample were studied using transmission ^{57}Fe Mössbauer spectroscopy on tourmaline at the Regional Centre of Advanced Technologies and Materials, Palacký University, Olomouc, Czech Republic. The spectrum of a powdered tourmaline sample (ground under acetone) was accumulated in a constant acceleration mode using a ^{57}Co in Rh source and 1024 channel detector at room temperature. The isomer shift was calibrated relative to an α-Fe foil. The spectrum was folded and fitted by Lorentz functions using the computer program CONFIT2000 (Žák and Jirásková 2006). The resulting five absorption doublets (Fig. 3b) indicate very low amounts of Fe^{3+}, quantified at 0.05(3) Fe^{3+}/Fe_{Tot} ratio (Table 5).

Micro-laser induced breakdown spectroscopy

For the holotype specimen, Li analysis was performed using 110 mJ of energy per pulse by double-pulse Q-Switched (Nd-YAG, λ = 1064 nm) laser with a 1 μs delay between the two pulses. The small spot size (7–10 μm) was obtained using a petrographic optical microscope (objective lens 10X NA 0.25 WD 14.75 mm). The LIBS spectra were acquired by AvaSpec Fiber Optic Spectrometer (390–900 nm with 0.3 nm resolution) with a delay of 2 μs after the second pulse and were integrated for 1 ms. Quantitative data were obtained by generating a linear regression using the main Li emission line intensity (670.706 nm corresponding to resonance transition $1s^2\,2s > 1s^2\,2p$), which is particularly sensitive to Li amounts. The linear fit was made using spectra recorded on two NIST standard glasses (SRM 610 and 612) and three Li-bearing tourmaline samples from Filip et al. (2012), Grew et al. (2018), and Bosi et al. (2019d). The result corresponds to 0.42 wt% of Li_2O (Table 4).

Laser ablation-inductively coupled plasma-mass spectroscopy

For the co-type of celleriite, Li analysis was performed using a LA-ICP-MS at the Department of Chemistry, Masaryk University, Brno. It consists of a UP 213 (New Wave Research, Inc., Fremont, California, U.S.A.) laser-ablation system and

Table 5. Room-temperature ^{57}Fe Mössbauer parameters for celleriite from the Rosina Pegmatite, San Piero in Campo, Elba Island, Italy (holotype) and the Pikárec Pegmatite, Western Moravia, Czech Republic (co-type)

δ (mm/s)	ΔE_Q (mm/s)	Γ (mm/s)	Assignment	Area (%)
		Holotype		
1.09	2.47	0.36	$^{[6]}Fe^{2+}$	81
1.12	2.06	0.20	$^{[6]}Fe^{2+}$	6
1.12	1.45	0.42	$^{[6]}Fe^{2+}$	9
0.42	0.16	0.24	$^{[6]}Fe^{3+}$	4
		Co-type		
1.10	2.39	0.29	$^{[6]}Fe^{2+}$	41
1.10	2.56	0.23	$^{[6]}Fe^{2+}$	26
1.10	1.74	0.47	$^{[6]}Fe^{2+}$	25
1.09	1.32	0.17	$^{[6]}Fe^{2.5+}$	3
0.29	0.48	0.35	$^{[6]}Fe^{3+}$	5

Note: δ = center shift (with respect to an α-Fe foil); ΔE_Q = quadrupole splitting; Γ = full-width at half maximum; Area = absorption area. Errors were estimated at about ±0.02 mm/s for δ, ΔE_Q, and Γ, and no less than ±3% absolute for doublets areas.

an Agilent 7500 CE (Agilent Technologies, Santa Clara, California, U.S.A.) ICPMS spectrometer. A commercial Q-switched Nd:YAG laser ablation device works at the fifth harmonic frequency, which corresponds to the wavelength of 213 nm. Laser ablation was performed with laser spots of diameter 40 μm, laser fluence 3 J/cm^2, and repetition rate 10 Hz. Lithium and trace element contents were calculated using NIST SRM 610 and 612 standards and Si and Al (values from earlier EMP analysis from measured spots) were used as internal reference elements after baseline correction and integration of the peak area. The result corresponds to 0.26 wt% of Li_2O (Table 4).

Raman spectroscopy

The Raman spectrum of the co-type of celleriite was obtained from a thin section using a Horiba Labram HR Evolution spectrometer. This dispersive, edge-filter-based system was equipped with an Olympus BX 41 optical microscope, a diffraction grating with 600 grooves per mm, and a Peltier-cooled, Si-based CCD detector. After careful tests with different lasers (473, 532, and 633 nm), the 532 nm diode laser with the beam power of 20 mW at the sample surface was selected for spectra acquisition to minimize analytical artifacts. The Raman signal was collected in the range of 100–4000 cm^{-1} with a 100× objective (NA 0.9). The system was operated in the confocal mode with a beam diameter of ~1 μm. No visual damage to the analyzed surface was observed at these conditions after the excitation. Raman shift calibration was done using the Rayleigh line and low-pressure Ne-discharge lamp emissions. The wavenumber accuracy was ~0.5 cm^{-1} and the spectral resolution was ~2 cm^{-1}. Band fitting was completed after appropriate background correction, assuming combined Lorentzian-Gaussian band shapes using Voight function. Based on the equation of Kutzschbach et al. (2016), the broad band at 3365 cm^{-1} indicates presence of at least 0.11 apfu $^{[4]}$B (Fig. 4); the actual amount may be higher due to partial deviation of the crystal from the ideal direction perpendicular to **c**.

Determination of atomic fractions

In accordance with the structural data, the B^{3+} content was assumed to be stoichiometric (B = 3.00 apfu). The Fe oxidation state was determined by MS. All Mn was considered to be Mn^{2+} based on the MS results and Fe and Mn redox potential arguments. Lithium was determined by μ-LIBS (holotype) and LA-ICP-MS (co-type). The (OH) content and the formula were then calculated by charge balance with the assumption (T + Y + Z) = 15.00 apfu and 31 anions. The very good agreement between the number of electrons per formula unit (epfu) derived from EMP and SREF analysis (236.8 vs. 235.8 epfu for the holotype sample and 236.0 vs. 236.5 epfu for the co-type sample) supports the stoichiometric assumptions.

Determination of site population and mineral formula

The anion site populations in the studied samples follow the general preference suggested for tourmaline (e.g., Henry et al. 2011): the O(3) site (V position in the general formula) is occupied by $(OH)^-$, while the O(1) site (W position in the general formula) can be occupied by O^{2-}, $(OH)^-$, and F^-. The *T* site is occupied by Si and Al (for the holotype specimen) or B^{3+} (for the co-type specimen). The latter is supported by Raman spectroscopy (Fig. 4). The cation distribution over the *Y* and *Z* sites has been optimized according to the procedure of Bosi et al. (2017) and the ionic radii of Bosi (2018). More specifically, the site distribution of Al, Fe^{3+}, Mn^{2+}, and Fe^{2+} was obtained by minimizing the residuals between the calculated and observed structural data [such as bond distance, bond valence, site scattering expressed in terms of mean atomic number (m.a.n.)] by using a least-squares program. Lithium and the minor amounts of Ti and Zn were fixed at the *Y* site, whereas the minor amount of Mg was fixed at *Z*. The resulting empirical crystal-chemical formulas for the studied samples are as follows:

$$^{X}(\square_{0.58}Na_{0.42})_{\Sigma 1.00}{}^{Y}(Mn^{2+}_{1.10}Fe^{2+}_{0.16}Al_{1.45}Fe^{3+}_{0.01}Li_{0.28}Ti_{0.01})_{\Sigma 3.00}{}^{Z}(Al_{5.70}Mn^{2+}_{0.29}Mg_{0.01})_{\Sigma 6.00}[{}^{T}(Si_{5.99}Al_{0.01})_{\Sigma 6.00}O_{18}](BO_3)_3(OH)_3{}^{W}[(OH)_{0.65}F_{0.03}O_{0.32}]_{\Sigma 1.00}$$ (holotype)

and

$$^{X}(\square_{0.51}Na_{0.49})_{\Sigma 1.00}{}^{Y}(Mn^{2+}_{0.81}Fe^{2+}_{0.50}Zn^{2+}_{0.04}Al_{1.46}Fe^{3+}_{0.04}Li_{0.17})_{\Sigma 3.00}{}^{Z}(Al_{5.91}Mn^{2+}_{0.09})_{\Sigma 6.00}[{}^{T}(Si_{5.75}B_{0.25})_{\Sigma 6.00}O_{18}](BO_3)_3(OH)_3{}^{W}[(OH)_{0.35}F_{0.17}O_{0.48}]_{\Sigma 1.00}$$ (co-type)

The observed data and those calculated from the optimized site populations are in excellent agreement (Table 6). The robustness of these site populations was confirmed by another optimization procedure (Wright et al. 2000), which led to very similar results. Of particular interest is the refined *Z*-site occupancy value of the holotype specimen (Online Materials[1] CIF and Table 6). It is consistent with the occurrence of minor amounts of cations (up to 0.3 apfu), such as Mn, with

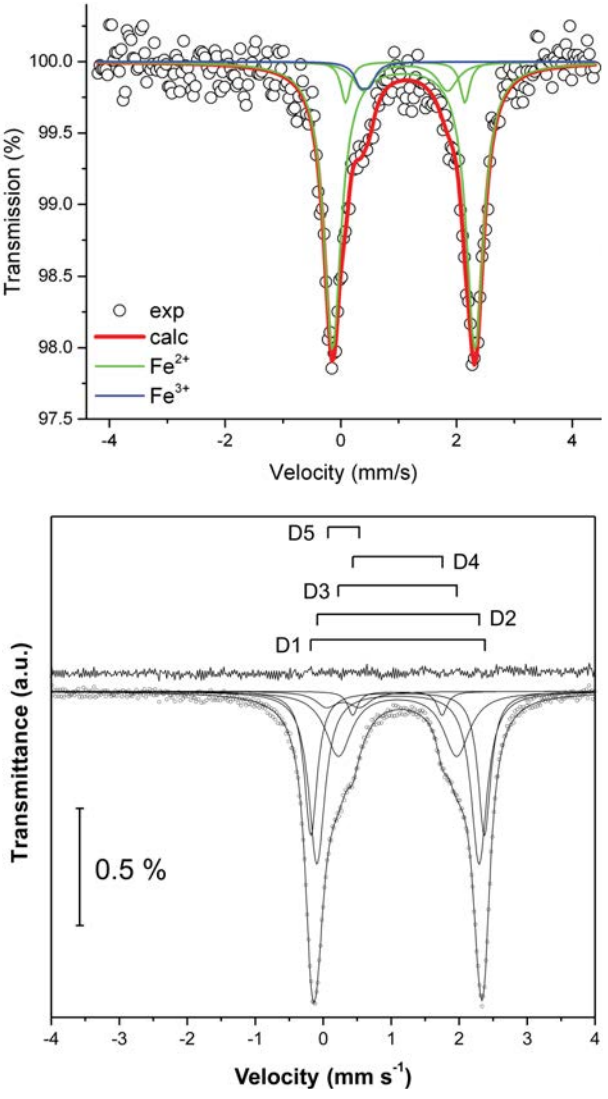

Figure 3. Room-temperature ^{57}Fe Mössbauer spectrum for celleriite. (**a**) The holotype specimen from the Rosina pegmatite, San Piero in Campo, Elba Island (Italy). (**b**) The co-type specimen from the Pikárec pegmatite, western Moravia, Czech Republic. (Color online.)

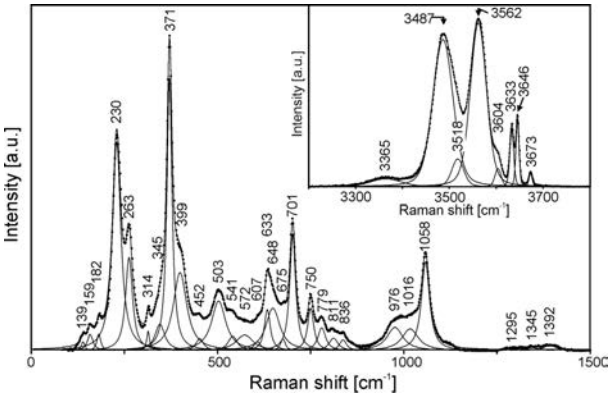

Figure 4. Raman spectrum for the co-type celleriite specimen from the Pikárec pegmatite, western Moravia, Czech Republic.

atomic numbers larger than Al: *Z*-m.a.n. = 13.47(8) is, in fact, significantly larger than the expected value for a *Z* site fully occupied by Al (*Z*-m.a.n. = 13). The latter is corroborated by the refined <*Z*-O> value (1.919 Å), which reflects the presence of cations larger than Al, such as Mn, when compared to the typical <*Z*-O> values observed for a *Z* site fully occupied by Al (1.902–1.913 Å; Bosi and Andreozzi 2013). Online Materials[1] Table OM1 reports the weighted bond valences.

Classification, end-member formula, and relation to other species

For classification purposes, the previously reported site allocation of ions has to be recast in an ordered formula with the *Z* site fully occupied by Al (Henry et al. 2011) to overcome the issues of uncertainty associated with cation order-disorder across *Y* and *Z*:

$^{X}(\square_{0.58}Na_{0.42})_{\Sigma1.00}{}^{Y}(Mn^{2+}_{1.39}Fe^{2+}_{0.16}Mg_{0.01}Al_{1.14}Fe^{3+}_{0.01}Li_{0.28}Ti_{0.01})_{\Sigma3.00}{}^{Z}Al_6[{}^{T}(Si_{5.99}Al_{0.01})_{\Sigma6.00}O_{18}](BO_3)_3(OH)_3{}^{W}[(OH)_{0.65}F_{0.03}O_{0.32}]_{\Sigma1.00}$ (holotype)

$^{X}(\square_{0.51}Na_{0.49})_{\Sigma1.00}{}^{Y}(Mn^{2+}_{0.90}Fe^{2+}_{0.50}Zn^{2+}_{0.04}Al_{1.36}Fe^{3+}_{0.04}Li_{0.17})_{\Sigma3.00}{}^{Z}Al_6[{}^{T}(Si_{5.75}B_{0.25})_{\Sigma6.00}O_{18}](BO_3)_3(OH)_3{}^{W}[(OH)_{0.35}F_{0.17}O_{0.48}]_{\Sigma1.00}$ (co-type)

These compositions are consistent with a tourmaline belonging to *X*-site vacant group, subgroup 1 (Henry et al. 2011): it is vacancy-dominant at the X position of the general formula of tourmaline $XY_3Z_6T_6O_{18}(BO_3)_3V_3W$ and hydroxy-dominant at W with $(OH+F)^- > O^{2-}$ and $(OH) \gg F$. Aluminum is the dominant cation at the *Z* site, whereas the valency-imposed double site-occupancy for the *Y* site is required to obtain a charge-balanced end-member composition. In this regard, we can consider the IMA-CNMNC rules (Bosi et al. 2019a, 2019b) and explore the resulting two possible end-member charge arrangements consistent with the composition:

$^{X}0\,{}^{Y}(2^{+}_{2}3^{+})\,{}^{Z}3^{+}_{6}({}^{T}4^{+}_{6}2^{-}_{18})({}^{B}3^{+}2^{-}_{3})_3\,{}^{O(3)}1^{-}_{3}\,{}^{O(1)}1^{-}$
$^{X}0\,{}^{Y}(3^{+}_{2}1^{+})\,{}^{Z}3^{+}_{6}({}^{T}4^{+}_{6}2^{-}_{18})({}^{B}3^{+}2^{-}_{3})_3\,{}^{O(3)}1^{-}_{3}\,{}^{O(1)}1^{-}$

where O(3) ≡ V and O(1) ≡ W. The replacement of most formal charges with the corresponding dominant constituents at the sites leads to:

$^{X}\square\,{}^{Y}(2^{+}_{2}3^{+})\,{}^{Z}Al_6({}^{T}Si_6O_{18})({}^{B}BO_3)_3\,{}^{O(3)}(OH)_3\,{}^{O(1)}(OH)$
$^{X}\square\,{}^{Y}(3^{+}_{2}1^{+})\,{}^{Z}Al_6({}^{T}Si_6O_{18})({}^{B}BO_3)_3\,{}^{O(3)}(OH)_3\,{}^{O(1)}(OH)$

Of particular interest is the site-total-charge at the *Y* sites (=+7), which suggests two possible charge and atomic arrangements compatible with +7 and the chemical composition for the holotype specimen:

$^{Y}(2^{+}_{2}3^{+})^{\Sigma7+} \rightarrow {}^{Y}(2^{+}_{2}3^{+})_{0.78} \rightarrow {}^{Y}(2^{2+}_{1.56}Al^{3+}_{0.78}) = 2.34$ apfu (limited by 2^+ contents);

$^{Y}(3^{+}_{2}1^{+})^{\Sigma7+} \rightarrow {}^{Y}(3^{+}_{2}1^{+})_{0.28} \rightarrow {}^{Y}(Al^{3+}_{0.56}Li^{+}_{0.28}) = 0.85$ apfu (limited by Li contents).

As a result, and in accordance with the dominant-valency rule, the proportion of the arrangement $^{Y}(2^{+}_{1.56}Al^{3+}_{0.78})$ is greater than the proportion of $^{Y}(Al^{3+}_{0.56}Li^{+}_{0.28})$. In accordance with the dominant-constituent rule, Mn^{2+} prevails among the divalent cations (1.39 Mn^{2+} apfu > 0.10 Fe^{2+} > 0.01 Mg^{2+}). Thus, the atomic arrangement $^{Y}(Mn^{2+}_{2}Al)$ is the dominant one in the holotype specimen from Rosina pegmatite, San Piero in Campo, Elba Island (Italy): $^{Y}(Mn^{2+}_{2}Al)_{0.695} = 2.09$ apfu, corresponding to ca. 70% of the site occupancy. Similar arguments apply to the co-type of celleriite form Pikárec pegmatite, western Moravia (Czech Republic): as the proportion of the charge arrangement $^{Y}(2^{+}_{2}3^{+})_{0.70} = 2.10$ apfu is larger than the proportion of $^{Y}(3^{+}_{2}1^{+})_{0.17} = 0.51$ apfu and $Mn^{2+} > Fe^{2+} > Zn^{2+}$, the dominant atomic arrangement is $^{Y}(Mn^{2+}_{2}Al)_{0.45}$ (=1.35 apfu). Therefore, Mn^{2+} is dominant at the *Y* site and the end-member composition can be represented as $\square(Mn^{2+}_{2}Al)Al_6(Si_6O_{18})(BO_3)_3(OH)_3(OH)$, which also requires Al

Table 6. Optimized cation site populations (atoms per formula unit), mean atomic numbers, and mean bond lengths (Å) for celleriite from the Rosina Pegmatite, San Piero in Campo, Elba Island, Italy (holotype) and the Pikárec Pegmatite, Western Moravia, Czech Republic (co-type)

	Holotype: site population	Mean atomic number		Mean bond length	
		Observed	Calculated	Observed	Calculated
X	0.58 □ + 0.42 Na	4.70(8)	4.68		
Y	1.10 Mn^{2+} + 0.16 Fe^{2+} + 1.45 Al + 0.01 Fe^{3+} + 0.28 Li + 0.01 Ti^{4+}	17.11(15)	17.19	2.031	2.033[a]
Z	5.70 Al + 0.29 Mn^{2+} + 0.01 Mg	13.47(8)	13.58	1.919	1.917[a]
T	5.99 Si + 0.01 Al	14[b]	14.00		
B	3 B	5[b]	5		
	Co-type: site population				
X	0.51 □+ 0.49 Na	5.36(5)	5.39		
Y	0.81 Mn^{2+} + 0.50 Fe^{2+} + 0.04 Zn + 1.46 Al + 0.04 Fe^{3+} + 0.17 Li	18.11(11)	18.19	2.026	2.031[a]
Z	5.91 Al + 0.09 Mn^{2+}	13.10(5)	13.18	1.912	1.908[a]
T	5.75 Si + 0.25 B	13.74(5)	13.63		
B	3 B	5[b]	5		

[a] Calculated from the empirical ionic radii (in Å) of Bosi (2018): Al = 0.547, Fe^{3+} = 0.675, Fe^{2+} = 0.776, Mn^{2+} = 0.809, Zn = 0.740, Li = 0.751, Ti = 0.605; the mean Y and Z anion radii are functions of constituent-anion radius (1.360 and 1.357, respectively).
[b] Fixed in the final stages of refinement.

at the *Y* site for charge-balance reasons (valency-imposed double-site occupancy). Since no tourmalines have yet been proposed with this end-member composition, the studied tourmalines can be classified as a new species with the name celleriite. In the vacant-subgroup 1 (Henry et al. 2011), celleriite is related to foitite and magnesio-foitite by the homovalent substitutions $Mn^{2+} \leftrightarrow Fe^{2+}$ and $Mn^{2+} \leftrightarrow Mg^{2+}$, respectively; properties of the three tourmalines are compared in Table 7. The heterovalent substitution $2Mn^{2+} \leftrightarrow Al^{3+} + Li^{+}$ relates celleriite to rossmanite (Fig. 5).

Geological and formation environment of celleriite

Holotype

Celleriite on Elba Island occurs in the Rosina pegmatite, which is located a few hundred meters south of the San Piero in Campo village, close to several other historic pegmatitic mineral localities such as "Prado," "Masso Foresi," "Fonte del Prete," and "Facciatoia" (Orlandi and Pezzotta 1996). These above-mentioned historic localities were mined during the 19th Century, whereas the Rosina pegmatite was discovered on private land by one of the authors (F.P.) in early 1990 and only started to be mined for collectibles and for specimens suitable for use in scientific research in 1992. From 2013 to 2016, the locality was included in a Research Permit of industrial purposes for Li and Rb mineralization in the pegmatite field that occurs along the eastern border zone of the Monte Capanne pluton in west Elba. At present, part of the Rosina pegmatite is still in place, and the locality is included in the didactic field visits organized by the Mineralogy Museum "Luigi Celleri" (MUM) of San Piero in Campo. The Rosina pegmatite is hosted in porphyritic monzogranite at the eastern border of the monzogranitic Mount Capanne pluton (7.4–6.9 Ma; Barboni et al. 2015). The pegmatite has a complex shape, trends roughly N-S, and has a variable dip angle of 40–75° W. The major productive section of the body is approximately 14 m long and is 0.6–2.1 m wide. The shallowest portions of the pegmatite body are the widest ones and are characterized by mostly aplitic textures with minor coarse-grained pegmatitic lenses. At greater depths, the body becomes more pegmatitic and divides into two major veins that are interconnected by several small veinlets. The Rosina pegmatite belongs to the LCT family, is strongly miarolitic with cavities >1 m in length, and is significantly asymmetric in terms of its textures, mineralogy and geochemistry. Textural asymmetries are evident in the pegmatitic portions: the axial core-miarolitic zone, which is rich in lepidolite, petalite, and pollucite, divides the body into a medium-grained lower section enriched in albite with minor K-feldspar, plus quartz, spessartine, and tourmaline in comb texture, together with patches of sekaninaite and an upper coarse-grained section enriched in K-feldspar with minor albite, quartz and tourmaline. This is evidenced by the composition of tourmaline as well as the occurrence of other geochemically evolved minerals such as petalite and pollucite. Cavities found at shallower levels contain mostly dark-colored tourmaline (from schorl to Fe-rich elbaite with variable Mn-contents to foitite) together with pale-blue beryl (aquamarine variety) and spessartine. Cavities found at deeper levels contain abundant polychrome and rose tourmaline, pink beryl (morganite variety), petalite, and pollucite.

Celleriite was found in a relatively large tabular cavity (ca. 100 × 70 × 25 cm) that occurs in an intermediate zone of the body. This cavity was discovered during mining performed in 2008. It displays the typical asymmetric distribution of the minerals: the roof is mostly covered by K-feldspar crystals, with quartz, minor albite and petalite, rare tourmaline crystals, and several pink beryl crystals, while the floor is rich in albite, petalite, quartz and drusy tourmalines, with locally abundant pollucite. Tourmaline crystals grew in the cavity in the direction of the analogous pole, ranging in length from approximately 1–3 cm with a diameter of up to 1 cm. The crystals are olive-green to yellow-green in color and are all characterized by a darker purplish-bluish-gray termination. Chemical analyses revealed an elbaite to fluor-elbaite composition along the crystal and mostly celleriite composition at the termination. The source crystal of celleriite shows compositional zoning from celleriite to Mn-rich, Fe^{2+}-bearing elbaite, fluor-elbaite and scarce rossmanite (Figs. 2a and 2b).

Co-type

The elbaite-subtype pegmatite from Pikárec near Křižanov, situated ~1.5 km S of the village, forms northwest-southeast-trending subvertical dike ca. 3 m thick and 50–70 m long, cutting amphibolite. From the contact inward, the pegmatite consists of the following units (zones): (1) thin, coarse-grained (~1–2 cm) outer granitic unit (Plg+Kfs+Qz+Bt±Tur) that evolves gradually into volumetrically dominant (2) medium- to coarse-grained (0.5 to 3 cm) graphic unit (Kfs+Qz > Ab+Qz). It locally contains biotite in its outermost parts where graphic textures are poorly developed. Very abundant black tourmaline is present in several morphological types in this unit; it is locally associated with Grt+Qz graphic intergrowths. The graphic unit evolves to masses of (3) pale brown to orange blocky K-feldspar (up to 10 cm) closely associated with or replaced by (4) bluish, medium-grained albite (albite unit), and (5) small masses of quartz in the central part of the dike. Small (6) pockets, up to

Table 7. Comparative data for the holotype specimens of celleriite, foitite, and magnesio-foitite

	Celleriite[a]	Foitite[b]	Magnesio-foitite[c]
a (Å)	15.9518(4)	15.967(2)	15.884(4)
c (Å)	7.1579(2)	7.126(1)	7.178(3)
V (Å^3)	1577.38(9)	1573.3(4)	1568.0(6)
Space group	*R*3*m*	*R*3*m*	*R*3*m*
Optic sign	Uniaxial (–)	Uniaxial (–)	Uniaxial (–)
ω	1.643(1)	1.664(1)	1.650
ε	1.628(1)	1.642(1)	1.624
Streak	White	Grayish-white	Not reported
Color	From violet to gray-blue	Bluish black	Pale bluish gray
Pleochroism	O = pale violet E = light gray-blue	O = pale lavender E = dark blue	O = gray-blue E = pale lavender
Strong lines in the powder XRD pattern *d* (Å) (I_{meas}, %)	2.573 (100) 3.983 (88) 4.210 (60) 3.453 (55) 2.943 (55) 6.345 (45)	2.573 (100) 3.452 (91) 6.338 (84) 2.944 (71) 4.212 (48) 3.989 (38)	2.567 (100) 3.969 (100) 4.211 (90) 2.949 (70) 6.366 (60) 3.471 (60)
Reference	This work	MacDonald et al. (1993)	Hawthorne et al. (1999)

Note: The pleochroism reported in MacDonald et al. (1993) is anomalous. All other tourmalines reported so far in literature display a reverse pleochroic scheme with O > E.

[a] $\square(Mn_2^{2+}Al)Al_6(Si_6O_{18})(BO_3)_3(OH)_3(OH)$.

[b] $\square(Fe_2^{2+}Al)Al_6(Si_6O_{18})(BO_3)_3(OH)_3(OH)$.

[c] $\square(Mg_2Al)Al_6(Si_6O_{18})(BO_3)_3(OH)_3(OH)$.

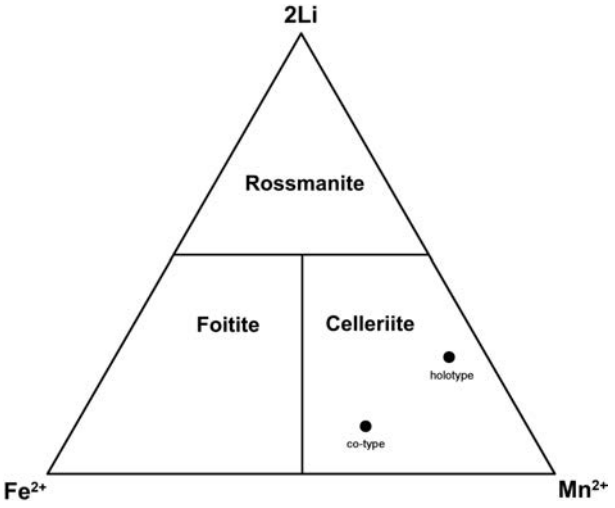

Figure 5. Dominant occupancy of the *Y* site with the *Z* site = Al in *X*-site vacant group tourmaline. Plot of celleriite compositions on the Fe^{2+}-Mn^{2+}-2Li diagram. The holotype specimen is from the Rosina pegmatite, San Piero in Campo, Elba Island, Italy; the co-type of celleriite is from the Pikárec pegmatite, western Moravia, Czech Republic.

1–2 dm^3 in size, are spatially associated with the units (3), (4), and (5); the pockets (6) are lined with crystals of K-feldspar, smoky quartz, albite, and polychrome Li-bearing tourmaline.

Along with major (Kfs, Plg, Ab, Qz), minor (Tur, Bt) and common accessory (Grt, Ap, löllingite) pegmatite constituents, several rare accessory minerals [columbite-(Mn), tantalite-(Mn), cassiterite, microlite, zircon, pollucite] were identified within the albite unit (Zahradníček 2012; Zahradníček and Novák 2012). Rare equidimensional grains of colorless to pinkish beryl, up to 1 cm in size, occur in albite that is close to pockets. Garnet is present as two textural and compositional types: graphic intergrowths of Qz+Grt ($Sps_{85–68}Alm_{15–31}Grs_{0–1}$) up to 3 cm in size in the inner part of the graphic unit, and very rare subhedral orange-red grains of spessartine ($Sps_{89–91}Alm_{9–11}$), up to 1 cm in size, in albite close to the pockets. Very rare small flakes of polylithionite and muscovite were found in pockets, the former also exceptionally in albite (Zahradníček and Novák 2012).

Tourmaline is present in a variety of morphological and paragenetic types. Rare, black prismatic crystals and their aggregates, up to 3 cm in size, occur in the outermost parts of the graphic unit. Black tourmaline in graphic (pseudographic) intergrowths with quartz is by far the most abundant morphology forming at least ~90% by volume of tourmaline in the pegmatite body. Aggregates of these intergrowths can reach up 15 cm in length, whereas the diameter of the individual tourmaline grains in the intergrowths varies from ~1–10 mm. The Qz+Tur intergrowths typically contain a larger tourmaline crystal in the center; they coarsen toward the pegmatite core and may evolve to large conical crystals of black tourmaline up to 3 cm long. The conical crystals occur in the innermost part of the graphic unit and blocky feldspar, at the contact with the albite unit and pockets, and are locally rimmed by pink tourmaline. The pockets contain short prismatic crystals of zoned tourmaline (greenish-black to deep red to pink) that are up to 5 cm long and commonly rooted at the top of the conical black crystals mentioned above. The last tourmaline generation in the pockets occurs as aggregates of small, prismatic pink crystals (up to 3 mm long) that overgrow crystals of K-feldspar and albite. Other color varieties of tourmaline (green, blue) common in Li-bearing granitic pegmatites (e.g., Jolliff et al. 1986; Novák and Povondra 1995; Selway et al. 1999) are absent. Celleriite in the Pikárec pegmatite forms a transitional zone in the dark brownish-green core of tourmaline from the root of a pegmatite pocket. The source crystal of celleriite shows compositional zoning from celleriite to elbaite, princivalleite, and fluor-elbaite (Fig. 2c).

Petrogenesis of celleriite

At the type specimen locality (Rosina pegmatite, Elba Island, Italy), paragenetic observations of the cavity provide evidence that the celleriite overgrew the analogous termination of tourmaline crystals during the latest stages of the cavity evolution after an episode of rigid mechanical shock and fracturing of the cavity. This caused some crystals in the cavity, including some tourmalines, to break and formed thin fractures in the pegmatite around the cavity. Subsequently, celleriite grew not only at the analogous pole at the termination of the tourmaline crystals but also on top of the broken bases with identical composition and pattern of chemical variation.

Manganese enrichment in late-stage pocket tourmaline is a characteristic feature of elbaite-subtype pegmatites (e.g., Novák and Povondra 1995; Novotný et al. 2019), in addition to their strongly peraluminous (Galliski et al. 2012) or transitional varieties (e.g., Dixon et al. 2014; Čopjaková et al. 2015). The main distinction from the otherwise similar Mn-enrichment in lepidolite-subtype pegmatites is the lower content of fluxing elements such as F and P_2O_5 in the elbaite-subtype pegmatites. As a result, there is little lepidolite and Mn-rich apatite that would deplete the albitic melt in Mn. This is accompanied by relatively low-F content in elbaite-subtype pegmatites that typically remains below 0.5 apfu in tourmaline until the hydrothermal-metasomatic stage of pegmatite crystallization, which is characterized by fluor-elbaite to fluor-liddicoatite compositions (e.g., Novotný et al. 2019; Zahradníček 2012; Flégr 2016). Interestingly, it seems that the presence of common spessartine-almandine garnet in magmatic pegmatite units does not preclude high Mn-enrichment in late-stage primary tourmaline in pegmatite pockets (Zahradníček 2012; Flégr 2016; Novotný 2020). This conclusion is consistent with the study of Haralampiev and Grover (1993), in which the high partitioning of Mn into garnet was suggested to prevent the development of tsilaisite. In the case of the Elba Island pegmatites, spessartine garnet generally stored most of the Mn present in the pegmatitic melt and crystallized in core zones at a relatively early stage of geochemical evolution. In the pegmatite portions in which the cavities are characterized by a relatively low geochemical evolution (as evidenced by the occurrence of dark and Fe-rich tourmalines, pale blue beryl, and a lack of pollucite), spessartine crystallized as a late-stage mineral, forming well-shaped crystals on previously crystallized minerals such as quartz, feldspars, schorl, and beryl. Conversely, in the pegmatite portions where the degree of geochemical evolution of the core zone is very advanced (as evidenced by polychrome and pink tourmaline,

the beryl variety morganite, abundant petalite, pollucite, and lepidolite), spessartine occurs crystallized early, inside feldspars and quartz, and sparsely as a rim of crystals around the pocket. As for the highly geochemically evolved Elba Island pegmatites, in the relatively rare cases when spessartine is absent, tourmaline incorporates most of the Mn that was present in the pegmatitic melt. Its crystals display a strong Mn enrichment, reaching the compositions of tsilaisite and fluor-tsilaisite. When both spessartine and tourmaline are present, the Mn enrichment in tourmaline is not enough to achieve tsilaisite and fluor-tsilaisite compositions, but a late-stage tourmaline can form with strong Mn enrichment and reaching celleriite composition.

In the specific case of the Rosina pegmatite, spessartine is relatively abundant and tourmaline is not particularly enriched in Mn (MnO up to ~6 wt% in elbaite and fluor-elbaite). Nevertheless, in the pocket in which celleriite was discovered, a strong Mn enrichment occurred at the termination of the tourmaline crystals, in a growth sector that formed after a pocket rupture. Such a pocket rupture is evidenced by: (1) the formation of thin fractures penetrating from the cavity into the surrounding solid pegmatite; (2) partial collapse of quartz and feldspar crystal aggregates in the cavity; and (3) the rupture of some of the tourmaline crystals. An event such as this could be related to some brittle deformation due to tensional stress associated with, for instance, thermal contraction during cooling of the rock. It is associated with significant albitization of K-feldspar, corrosion of spessartine, and alteration of the few tapering crystals of biotite to white mica. Fracturing was followed by a recrystallization event, with overgrowth of quartz and feldspar crystals and the formation of significant dark overgrowths (mostly composed of celleriite) at the analogous poles of tourmaline crystals, both on the pedion faces of terminated crystals and the fracture surfaces of broken crystals. These phenomena of corrosion, alteration, and crystallization may be ascribed to the aggressive late-stage fluids from pegmatite pockets, which penetrated into the fractures and, because some B was still present, allowing for the formation of a late-stage tourmaline generation. A similar feature was noted in the Cruzeiro pegmatite with the development of fibrous tourmaline by Dutrow and Henry (2000). An additional piece of evidence for the occurrence of a late-stage enrichment of Mn in the cavities of Elba pegmatites, and, for instance, the Rosina pegmatite, is documented by the local crystallization of helvite (Pezzotta 2000).

Dark-terminations at the analogous pole of multicolored tourmaline crystals are quite characteristic for tourmalines of Elba Island pegmatites and are typically Fe^{2+}-rich (e.g., Orlandi and Pezzotta 1996). Although there is little documentation in the literature, the formation of such late-stage overgrowths in Elba tourmalines is likely due to partial re-opening of the geochemical system and the introduction of Fe, and possible minor quantities of other elements such as Mg and Ti, which were incorporated in earlier crystallized minerals. This new system is related to the hydrothermal alteration of these earlier crystallized minerals, such as biotite and sekaninaite. Systematic analyses of the dark terminations in Elba tourmalines indicate mostly foitite and rarely schorl composition (Pezzotta et al. 1996; Altieri 2019). In the case of the celleriite-bearing pocket, the relative abundance of spessartine in the surrounding solid pegmatite coupled with the scarcity of biotite and other Fe-rich minerals may account for a Mn-rich, Fe-poor source in the late-stage fluids. The latter was responsible for the crystallization of a relatively dark tourmaline overgrowth composed of celleriite in the Rosina pegmatite instead of the typical occurrence of foitite.

At the co-type specimen locality (Pikárec pegmatite, Czech Republic), a gradual, moderate increase of Mn and Al followed by a much more pronounced decrease of Fe at low-F and -Na levels seem to be a primary feature that is unrelated to the hydrothermal stage. The hydrothermal stage is characterized by fluor-elbaite composition with F, Na, and Al, and very low Fe and Mn (Fig. 2b; see also Zahradníček 2012). Therefore, locally extreme Mn content in the pegmatite albite zone combined with low-F and low-P_2O_5 contents seem to be the most significant factors controlling the formation of celleriite in the Pikárec pegmatite.

Implications

The formation of Mn-dominant tourmalines (celleriite, tsilaisite, and fluor-tsilaisite) requires specific geochemical conditions that are rare in nature. According to Simmons et al. (2011), the original pegmatite-forming melt (preferably a B-rich peraluminous melt) must be relatively low in Fe and enriched in Mn and B; moreover, during the early stages of crystallization, Fe must be removed, but abundant B and Mn must still be available when tourmaline crystallizes. In this regard, the occurrence of the new mineral celleriite provides an excellent example of a mineral species formed under unusual environmental conditions. Thus, celleriite appears to be valuable in understanding Earth as a complex, evolving system in which metasomatic fluid-rock interactions may lead to new mineral-forming environments, in particular for B minerals (Hazen and Ausubel 2016; Grew et al. 2016). Moreover, the crystal overgrowth of celleriite implies that while the dark termination—the so-called "Moor's head" textural type—is characteristic for the Elba Island pegmatites, it is not a feature exclusively produced by Fe enrichment but may also imply the presence of a Mn-dominant component.

Acknowledgments

Chemical analyses were completed with the kind assistance of M. Serracino, to whom the authors express their gratitude. The associate editor, E.S. Grew, the Technical Editor, and the reviewers, P. Bačík and D.J. Henry, are thanked for their constructive comments.

Funding

Funding by Sapienza University of Rome (Prog. Università 2018 to F. Bosi) and Deep Carbon Observatory (2016 to G.B. Andreozzi) are gratefully acknowledged. J.C., R.Š., R.Č., and M.N. acknowledge support from the project GAČR 17-17276S. The research was supported by an NSERC Discovery Grant to L.A.G. (funding reference 06434). Support from the John Jago Trelawney Endowment to the Mineral Sciences Department of the Natural History Museum of Los Angeles County to A.R.K. is acknowledged. Part of the data presented in this paper were obtained at CEITEC, Core Facility X-ray Diffraction, and Bio-SAXS supported by MEYS CR (LM2018127).

References cited

Ahmadi, S., Tahmasbi, Z., Khalaji, A.A., and Zal, F. (2019) Chemical variations and origin of tourmalines in laleh zar granite of Kerman (Southeast Iran). Periodico di Mineralogia, 88, 117–129.

Altieri, A. (2019) Evoluzione cristallochimica di tormaline delle pegmatiti a gemme dell'Isola d'Elba. Master thesis, Sapienza University of Rome, 129 p. (in Italian).

Andreozzi, G.B., Bosi, F., and Longo, M. (2008) Linking Mössbauer and structural parameters in elbaite-schorl-dravite tourmalines. American Mineralogist, 93, 658–666.

Andreozzi, G.B., Bosi, F., Celata, B., Capizzi, L.S., Stagno, V., and Beckett-Brown, C. (2020) Crystal-chemical behavior of Fe^{2+} in tourmaline dictated by structural

stability: insights from a schorl with formula $Na^{Y}(Fe^{2+}_{2}Al)^{Z}(Al_5Fe^{2+})(Si_6O_{18})(BO_3)_3(OH)_3(OH,F)$ from Seagull batholith (Yukon Territory, Canada). Physics and Chemistry of Minerals, 47, 25.

Barboni, M., Annen, C., and Schoene, B. (2015) Evaluating the construction and the evolution of upper crustal magma reservoirs with coupled U/Pb zircon geochronology and thermal modeling: A case study from the Mt. Capanne pluton (Elba, Italy). Earth and Planetary Science Letters, 432, 436–448.

Bosi, F. (2013) Bond-valence constraints around the O1 site of tourmaline. Mineralogical Magazine, 77, 343–351.

——— (2014) Bond valence at mixed occupancy sites. I. Regular polyhedra. Acta Crystallographica, B70, 864–870.

——— (2018) Tourmaline crystal chemistry. American Mineralogist, 103, 298–306.

Bosi, F., and Andreozzi, G.B. (2013) A critical comment on Ertl et al. (2012): "Limitations of Fe^{2+} and Mn^{2+} site occupancy in tourmaline: Evidence from Fe^{2+}- and Mn^{2+}-rich tourmaline. American Mineralogist, 98, 2183–2192.

Bosi, F., and Lucchesi, S. (2007) Crystal chemical relationships in the tourmaline group: structural constraints on chemical variability. American Mineralogist, 92, 1054–1063.

Bosi, F., Agrosì, G., Lucchesi, S., Melchiorre, G., and Scandale, E. (2005) Mn-tourmaline from island of Elba (Italy). Crystal chemistry. American Mineralogist, 90, 1661–1668.

Bosi, F., Skogby, H., Agrosì, G., and Scandale, E. (2012) Tsilaisite, $NaMn_3Al_6(Si_6O_{18})(BO_3)_3(OH)_3OH$, a new mineral species of the tourmaline supergroup from Grotta d'Oggi, San Pietro in Campo, island of Elba, Italy. American Mineralogist, 97, 989–994.

Bosi, F., Andreozzi, G.B., Agrosì, G., and Scandale, E. (2015) Fluor-tsilaisite, $NaMn_3Al_6(Si_6O_{18})(BO_3)_3(OH)_3F$, a new tourmaline from San Piero in Campo (Elba, Italy) and new data on tsilaisitic tourmaline from the holotype specimen locality. Mineralogical Magazine, 79, 89–101.

Bosi, F., Reznitskii, L., Hålenius, U., and Skogby, H. (2017) Crystal chemistry of Al–V–Cr oxy-tourmalines from Sludyanka complex, Lake Baikal, Russia. European Journal of Mineralogy, 29, 457–472.

Bosi, F., Naitza, S., Skogby, H., Secchi, F., Conte, A.M., Cuccuru, S., Hålenius, U., De La Rosa, N., Kristiansson, P., Charlotta Nilsson, E.J., Ros, L., and Andreozzi, G.B. (2018) Late magmatic controls on the origin of schorlitic and foititic tourmalines from late-Variscan peraluminous granites of the Arbus pluton (SW Sardinia, Italy): Crystal-chemical study and petrological constraints. Lithos, 308-309, 395–411.

Bosi, F., Hatert, F., Hålenius, U., Pasero, M., Miyawaki, R., and Mills, S.J. (2019a) On the application of the IMA-CNMNC dominant-valency rule to complex mineral compositions. Mineralogical Magazine, 83, 627–632.

Bosi, F., Biagioni, C., and Oberti, R. (2019b) On the chemical identification and classification of minerals. Minerals, 9, 591.

Bosi, F., Naitza, S., Secchi, F., Conte, A.M., Cuccuru, S., Andreozzi, G.B., Skogby, H., and Hålenius, U. (2019c) Petrogenetic controls on the origin of tourmalinite veins from Mandrolisai igneous massif (Central Sardinia, Italy): Insights from tourmaline crystal chemistry. Lithos, 342-343, 333–344.

Bosi, F., Skogby, H., and Hålenius, U. (2019d) Thermally induced cation redistribution in fluor-elbaite and Fe-bearing tourmalines. Physics and Chemistry of Minerals, 46, 371–383.

Bosi, F., Pezzotta, F., Altieri, A., Andreozzi, G.B., Ballirano, P., and Tempesta, G. (2020a) Celleriite, IMA 2019-089. CNMNC Newsletter. February 2020, Page 211. European Journal of Mineralogy, 32, 209–213.

Bosi, F., Pezzotta, F., Skobgy, H., Altieri, A., Hålenius, U., Tempesta, G., and Cempírek, J. (2020b) Princivalleite, IMA 2020-056. CNMNC Newsletter No. 58, December 2020. European Journal of Mineralogy, 32, https://doi.org/10.5194/ejm-32-645-2020.

Brese, N.E., and O'Keeffe, M. (1991) Bond-valence parameters for solids. Acta Crystallographica, B47, 192–197.

Cempírek, J., Houzar, S., Novák, M., Groat, L.A., Selway, J.B., and Šrein, V. (2013) Crystal structure and compositional evolution of vanadium-rich oxy-dravite from graphite quartzite at Bítovánky, Czech Republic. Journal of Geosciences, 58, 149–162.

Černý, P., London, D., and Novák, M. (2012) Granitic pegmatites as reflection of their sources. Elements, 8, 289–294.

Čopjaková, R., Škoda, R., Vašinová-Galiová, M., Novák, M., and Cempírek, J. (2015) Sc- and REE-rich tourmaline replaced by Sc-rich REE-bearing epidote-group mineral from the mixed (NYF+LCT) Kracovice pegmatite (Moldanubian Zone, Czech Republic). American Mineralogist, 100, 1434–1451.

Dixon, A., Cempírek, J., and Groat, L.A. (2014) Mineralogy and geochemistry of pegmatites on Mount Begbie, British Columbia. Canadian Mineralogist, 52, 129–164.

Dutrow, B.L., and Henry, D.J. (2000) Complexly zoned fibrous tourmaline, Cruzeiro mine, Minas Gerais, Brazil: A record of evolving magmatic and hydrothermal fluids. Canadian Mineralogist, 38, 131–143.

——— (2018) Tourmaline compositions and textures: reflections of the fluid phase. Journal of Geosciences, 63, 99–110.

Ertl, A., Hughes, J.M., Pertlik, F., Foit, F.F. Jr., Wright, S.E., Brandstatter, F., and Marler, B. (2002) Polyhedron distortions in tourmaline. Canadian Mineralogist, 40, 153–162.

Ertl, A., Henry, D.J., and Tillmanns, E. (2018) Tetrahedral substitutions in tourmaline: a review. European Journal of Mineralogy, 30, 465–470.

Filip, J., Bosi, F., Novák, M., Skogby, H., Tuček, J., Čuda, J., and Wildner, M. (2012) Redox processes of iron in the tourmaline structure: Example of the high-temperature treatment of Fe^{3+}-rich schorl. Geochimica et Cosmochimica Acta, 86, 239–256.

Flégr, T. (2016) Vývoj chemického složení turmalínů z elbaitového pegmatitu Řečice. M.S. thesis, Faculty of Science, Masaryk University, Brno (in Czech).

Foit, F.F. Jr. (1989) Crystal chemistry of alkali-deficient schorl and tourmaline structural relationships. American Mineralogist, 74, 422–431.

Gadas, P., Novak, M., Stanek, J., Filip, J., and Galiova, M.V. (2012) Compositional evolution of zoned tourmaline crystals from pockets in common pegmatites, the Moldanubian Zone, Czech Republic. Canadian Mineralogist, 50, 895–912.

Gagné, O.C., and Hawthorne, F.C. (2015) Comprehensive derivation of bond-valence parameters for ion pairs involving oxygen. Acta Crystallographica Section B, Structural Science, Crystal Engineering and Materials, B 71, 562–578.

Galliski, M.A., Marquez-Zavalia, M.F., Lira, R., Cempirek, J., and Skoda, R. (2012) Mineralogy and origin of the dumortierite-bearing pegmatites of Virorco, San Luis, Argentina. Canadian Mineralogist, 50, 873–894.

Grew, E.S., Bosi, F., Ros, L., Kristiansson, P., Gunter, M.E., Hålenius, U., Trumbull, R.B., and Yates, M.G. (2018) Fluor-elbaite, lepidolite and Ta-Nb oxides from a pegmatite of the 3000 MA Sinceni pluton, Swaziland: Evidence for lithium-cesium-tantalum (LCT) pegmatites in the Mesoarchean. European Journal of Mineralogy, 30, 205–218.

Grew, E.S., Krivovichev, S.V., Hazen, R.M., and Hystad, G. (2016) Evolution of structural complexity in boron minerals. Canadian Mineralogist, 54, 125–143.

Grice, J.D., and Ercit, T.S. (1993) Ordering of Fe and Mg in the tourmaline crystal structure: The correct formula. Neues Jahrbuch für Mineralogie Abhandlungen, 165, 245–266.

Haralampiev, A.G., and Grover, J. (1993) Synthesis experiments in the binary system tsilaisite–dravite, $Na(Mn_xMg_{1-x})_3Al_6(BO_3)_3Si_6O_{18}(OH)_4$, at $T = 375–700°$ and $P = 2000$ bars; does garnet control the occurrence of tourmaline? Geological Society of America Abstracts with Program, 25, 94–55.

Hawthorne, F.C., Selway, J.B., Kato, A., Matsubara, S., Shimizu, M., Grice, J.D., and Vajdak, J. (1999) Magnesiofoitite, $\square(Mg_2Al)Al_6(Si_6O_{18})(BO_3)_3(OH)_4$, a new alkali-deficient tourmaline. Canadian Mineralogist, 37, 1439–1443.

Hazen, R.M., and Ausubel, J.H. (2016) On the nature and significance of rarity in mineralogy. American Mineralogist, 101, 1245–1251.

Henry, D.J., and Dutrow, B.L. (1996) Metamorphic tourmaline and its petrologic applications. In E.S. Grew and L.M. Anvitz, Eds., Boron: Mineralogy, petrology and geochemistry, 33. 503–557. Reviews in Mineralogy and Geochemistry, Mineralogical Society of America, Chantilly, Virginia.

——— (2011) The incorporation of fluorine in tourmaline: Internal crystallographic controls or external environmental influences? Canadian Mineralogist, 49, 41–56.

Henry, D.J., Novák, M., Hawthorne, F.C., Ertl, A., Dutrow, B., Uher, P., and Pezzotta, F. (2011) Nomenclature of the tourmaline-supergroup minerals. American Mineralogist, 96, 895–913.

Jolliff, B.L., Papike, J.J., and Shearer, C.K. (1986) Tourmaline as a recorder of pegmatite evolution: Bob Ingersoll Pegmatite, Black Hills, South Dakota. American Mineralogist, 71, 472–500.

Kutzschbach, M., Wunder, B., Rhede, D., Koch-Müller, M., Ertl, A., Giester, G., Heinrich, W., and Franz, G. (2016) Tetrahedral boron in natural and synthetic HP/UHP tourmaline: Evidence from Raman spectroscopy, EMPA, and single-crystal XRD. American Mineralogist, 101, 93–104.

MacDonald, D.J., Hawthorne, F.C., and Grice, J.D. (1993) Foitite, $\square(Al,Fe^{3+})Al_6Si_6O_{18}(BO_3)_3(OH)_4$, a new alkali-deficient tourmaline: Description and crystal structure. American Mineralogist, 78, 1299–1303.

Mandarino, J.A. (1981) The Gladstone-Dale relationship. Part IV: The compatibility concept and its application. Canadian Mineralogist, 19, 441–450.

Merlet, C. (1994) An accurate computer correction program for quantitative electron probe microanalysis. Mikrochimica Acta, 114-115, 363–376.

Novák, M., and Cempírek, J., Eds. (2010) Granitic pegmatites and mineralogical museums in Czech Republic. IMA 2010 Field Trip Guide CZ2. Acta Mineralogica Petrographica Field Guide Series 6, Szeged, p. 1–56.

Novák, M., and Povondra, P. (1995) Elbaite pegmatites in the Moldanubicum: a new subtype of the rare-element class. Mineralogy and Petrology, 55, 159–176.

Novák, M., Povondra, P., and Selway, J.B. (2004) Schorl-oxy-schorl to dravite-oxydravite tourmaline from granitic pegmatites; examples from the Moldanubicum, Czech Republic. European Journal of Mineralogy, 16, 323–333.

Novák, M., Škoda, P., Filip, J., Macek, I., and Vaculovič, T. (2011) Compositional trends in tourmaline from intragranitic NYF pegmatites of the Třebíč Pluton, Czech Republic; electron microprobe, Mössbauer and LA-ICP-MS study. The Canadian Mineralogist, 49, 359–380.

Novotný, F. (2020) Mineralogy of the Dolní Rožínka elbaite-subtype pegmatite. M.S. thesis, Faculty of Science, Masaryk University, Brno (in Czech).

Novotný, F., Novák, M., and Cempírek, J. (2019) Chemical composition of tourmaline from the Dolní Rožínka elbaite pegmatite. Bulletin of Mineralogy and Petrology, 27, 38–45.

Orlandi, P., and Pezzotta, F. (1996) Minerali dell'Isola d'Elba, i minerali dei giacimenti metalliferi dell'Elba orientale e delle pegmatiti del Capanne, Monte Ed. Novecento Grafico, Bergamo, 248 pp (in Italian).
Pezzotta, F. (2000) Internal structures, parageneses and classification of the miarolitic (Li-bearing) complex pegmatites of Elba Island (Italy). Mineralogy and Petrology of Shallow Depth Pegmatites. Papers from the First International Workshop. Memorie Della Società Italiana di Scienze Naturali e Del Museo Civico di Storia Naturale di Milano, 30, 29–43.
Pezzotta, F., Hawthorne, F., Cooper, M.A., and Teerstra, D. (1996) Fibrous foitite from S. Piero in Campo, Elba, Italy. Canadian Mineralogist, 34, 741–744.
Pouchou, J.L., and Pichoir, F. (1991) Quantitative analysis of homogeneous or stratified microvolumes applying the model "PAP." In K.F.J. Heinrich and D.E. Newbury, Eds., Electron Probe Quantitation, p. 31–75. Plenum.
Selway, J.B., Novák, M., Černý, P., and Hawthorne, F.C. (1999) Compositional evolution of tourmaline in lepidolite-subtype pegmatites. European Journal of Mineralogy, 11, 569–584.
Sheldrick, G.M. (2015) Crystal structure refinement with SHELXL. Acta Crystallographica, C71, 3–8.
Simmons, W.B., Falster, A.U., and Laurs, B.M. (2011) A survey of Mn-rich yellow tourmaline from worldwide localities and implications for the petrogenesis of the granitic pegmatites. Canadian Mineralogist, 49, 301–319.
van Hinsberg, V.J., Henry, D.J., and Marschall, H.R. (2011a) Tourmaline: An ideal indicator of its host environment. Canadian Mineralogist, 49, 1–16.
van Hinsberg, V.J., Henry, D.J., and Dutrow, B.L. (2011b) Tourmaline as a petrologic forensic mineral: a unique recorder of its geologic past. Elements, 7, 327–332.
Wright, S.E., Foley, J.A., and Hughes, J.M. (2000) Optimization of site occupancies in minerals using quadratic programming. American Mineralogist, 85, 524–531.
Zahradníček, L. (2012) Vývoj textur a chemického složení zonálních turmalínů z elbaitového pegmatitu v Pikárci u Křižanova. M.S. thesis, Faculty of Science, Masaryk University, Brno (in Czech).
Zahradníček, L., and Novák, M. (2012) Lithium-bearing micas from elbaite-subtype pegmatites in the Western Moravia, Czech Republic. Acta Musei Moraviae, Scientiae geologicae. In Czech with English Summary, 97, 25–37.
Žák, T., and Jirásková, Y. (2006) CONFIT: Mössbauer spectra fitting program. Surface and Interface Analysis, 38, 710–714.

Manuscript received September 21, 2020
Manuscript accepted January 2, 2021
Manuscript handled by Edward S. Grew

Endnote:

[1]Deposit item AM-22-17818, Online Materials. Deposit items are free to all readers and found on the MSA website, via the specific issue's Table of Contents (go to http://www.minsocam.org/MSA/AmMin/TOC/2022/Jan2022_data/Jan2022_data.html). The CIF has been peer reviewed by our Technical Editors.